

## SYNTHETIC BIOLOGY

## Probiotic-guided CAR-T cells for solid tumor targeting

Rosa L. Vincent<sup>1†</sup>, Candice R. Gurbatri<sup>1†</sup>, Fangda Li<sup>2</sup>, Ana Vardoshvili<sup>1</sup>, Courtney Coker<sup>1</sup>, Jongwon Im<sup>1</sup>, Edward R. Ballister<sup>1,2</sup>, Mathieu Rouanne<sup>2,3</sup>, Thomas Savage<sup>2</sup>, Kenia de los Santos-Alexis<sup>2</sup>, Andrew Redenti<sup>1,2</sup>, Leonie Brockmann<sup>2</sup>, Meghna Komaranchath<sup>1</sup>, Nicholas Arpaia<sup>2,3</sup>, Tal Danino<sup>1,3,4\*</sup>

A major challenge facing tumor-antigen targeting therapies such as chimeric antigen receptor (CAR)–T cells is the identification of suitable targets that are specifically and uniformly expressed on heterogeneous solid tumors. By contrast, certain species of bacteria selectively colonize immune-privileged tumor cores and can be engineered as antigen-independent platforms for therapeutic delivery. To bridge these approaches, we developed a platform of probiotic-guided CAR-T cells (ProCARs), in which tumor-colonizing probiotics release synthetic targets that label tumor tissue for CAR-mediated lysis *in situ*. This system demonstrated CAR-T cell activation and antigen-agnostic cell lysis that was safe and effective in multiple xenograft and syngeneic models of human and mouse cancers. We further engineered multifunctional probiotics that co-release chemokines to enhance CAR-T cell recruitment and therapeutic response.

**A**lthough there has been marked success in the use of chimeric antigen receptor (CAR)–T cells for hematological malignancies, effective targeting of solid tumors has been limited. A key challenge of antigen-targeted cell therapies relates to the expression patterns of the antigen itself, which makes the identification of optimal targets for solid tumor cell therapies an obstacle for the development of new CARs (1–3). Few tumor-associated antigens (TAAs) identified on solid tumors are tumor restricted, and thus, they carry a high risk of fatal on-target, off-tumor toxicity because of cross-reactivity against proteins found in vital tissues (4–6). Moreover, if a safe target can be identified, TAAs are often heterogeneously expressed, and selection pressures from targeted therapies ultimately lead to antigen-negative relapse (7, 8). Emerging strategies to address the antigen bottleneck have focused on improving CAR-T cells with additional genetic circuitry (9–11), modulatory proteins (12–17), or combinations with nanoproteins and oncolytic viruses (18–21).

Whereas CAR-T cells require considerable engineering to target and infiltrate solid tumors, bacteria can selectively colonize immune-privileged tumor cores and preferentially grow within hostile hypoxic and necrotic tumor microenvironments (TMEs) (22). Indeed, a multitude of patient studies have shown that different tumor types host different tumor microbiomes (23–25). To take advantage of these inherent properties, several groups have established an array of synthetic gene circuits to engineer a new class of prokaryotic cell ther-

apy (26, 27). These approaches have used engineered bacteria as intratumoral bioreactors that continually produce a range of payloads, which results in tumor regression and mitigation of systemic side effects (28–31). Notably, clinical trials with engineered bacteria have reported minimal toxicities in patients with solid tumors, although these have yet to demonstrate considerable clinical efficacy across a broad range of indications (32–34).

In this work, we bridge the complementarity of these two cell therapies in a platform of probiotic-guided CAR-T cells (ProCARs), whereby T cells are engineered to sense and respond to synthetic CAR targets that are released by tumor-colonizing, probiotic bacteria. This approach leverages the antigen independence of tumor-seeking microbes to create a combined cell therapy platform that broadens the scope of CAR-T cell therapy to include difficult-to-target tumors.

## Results

## Synthetic CAR targets “Tag” tumor cells for lysis by ProCAR-T cells

To create a TAA-independent ProCAR platform, we engineered a well-characterized probiotic strain, *Escherichia coli* Nissle 1917 (EcN), which is equipped with a genomically integrated, synchronized lysis circuit (SLIC) for quorum-regulated delivery of synthetic CAR targets directly to the tumor core. With this system, bacterial growth reaches a critical population density exclusively within the niche of the solid TME and subsequently triggers lysis events that cyclically release genetically encoded payloads *in situ* (30, 35).

First, we designed extracellular proteins that can “tag” components of the TME for CAR-mediated lysis. Specifically, we fused a homodimer of superfolder green fluorescent protein (sfGFP) (diGFP)—previously shown to mediate CAR-T cell responses to soluble, dimeric ligands (36)—to the heparin-binding domain (HBD) of placenta growth factor-2 (PlGF-2<sub>123–144</sub>) (37). Notably, the HBD from PlGF-2 broadly anchors to collagens, fibronectins, and heparan sul-

fate proteoglycans (HSPGs) that are found in high abundance on most solid tumors within the dense extracellular matrix (ECM) of the tumor stroma (38). We hypothesized that heparin-binding CAR targets (“Tags”) would benefit the ProCAR system twofold: (i) by limiting diffusion beyond ECM-dense tumor margins, which thereby enhances the safety of the system, and (ii) by facilitating CAR polarization akin to conventional CAR and T cell receptor signaling (39), which thus results in greater antitumor activity (Fig. 1A).

To achieve stable protein expression *in vivo*, we expressed the CAR targets under a constitutive *tac* promoter from an *Axe/Txe* stabilized plasmid (40) (fig. S1, A and B) and confirmed efficient collagen binding of Tags after His-tag-mediated protein purification (fig. S2, A to C). Next, we composed a GFP-specific CAR from an sfGFP-binding nanobody sequence (41) linked to CD28 and CD3 $\zeta$  intracellular signaling domains by a short immunoglobulin G4 (IgG4) hinge for coexpression with an mScarlet reporter. With this, we were able to monitor the transduction efficiency of human T cells by mScarlet expression and confirm surface expression through CAR receptor binding to purified, monomeric sfGFP (Fig. 1B).

We first sought to measure CAR-T cell activation in the presence of each purified sfGFP variant in comparison to MDA-MB-468 cells engineered to express a membrane-bound form of sfGFP (“mbGFP”) (fig. S1, C to E). Here, we found that GFP CAR-T cells (GFP28z) comparatively activated in response to collagen-bound Tags, moderately activated in response to soluble diGFP, and remained unchanged by exposure to monomeric sfGFP (Fig. 1C). Quantification of CD69 surface expression demonstrated dose-dependent activation, with increased levels observed in response to collagen-bound Tags (figs. S2D and S3A). We additionally evaluated intracellular levels of T helper cell 1 (T<sub>H</sub>1) proinflammatory cytokines, for which GFP28z displayed higher frequencies of polyfunctional CD8<sup>+</sup> T cells that produce interferon- $\gamma$  (IFN- $\gamma$ ) and tumor necrosis factor- $\alpha$  (TNF $\alpha$ ) in response to either collagen-bound Tags or mbGFP (fig. S3, B to D). Both diGFP and collagen-bound Tag yielded similar fold expansion after a single exposure to either target (fig. S3E).

Although previous studies did not observe target cell lysis in response to soluble ligands (36), we hypothesized that Tags may facilitate the lysis of cancer cells by binding to membrane-spanning matrix proteins (42). To assess cell surface interaction, we incubated untransduced (UT) T cells, triple negative breast cancer (TNBC), and ovarian cancer cell lines with diGFP or Tag variants and demonstrated that Tags robustly coat the surface of both cancer cell lines but do not bind the surface of rested or activated T cells (Fig. 1D and fig. S4A). Moreover, we did not observe significant surface

<sup>1</sup>Department of Biomedical Engineering, Columbia University, New York, NY 10027, USA. <sup>2</sup>Department of Microbiology and Immunology, Vagelos College of Physicians and Surgeons of Columbia University, New York, NY 10032, USA. <sup>3</sup>Herbert Irving Comprehensive Cancer Center, Columbia University, New York, NY 10032, USA. <sup>4</sup>Data Science Institute, Columbia University, New York, NY 10027, USA.

\*Corresponding author. Email: td2506@columbia.edu

†These authors contributed equally to this work.



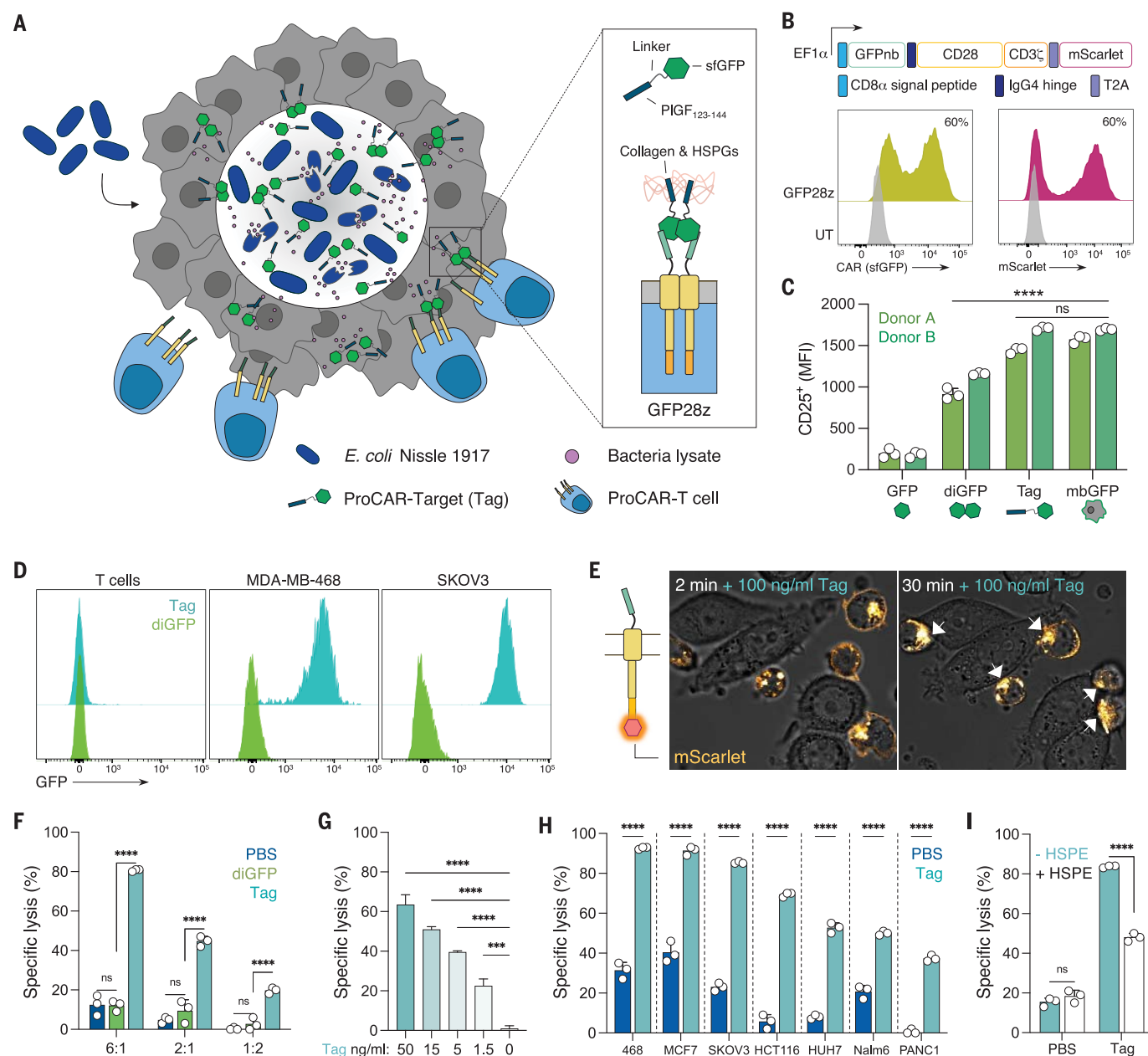


**Fig. 1. Synthetic CAR targets “Tag” tumor cells for lysis by ProCAR-T cells in situ.** (A) Schematic demonstrating the ProCAR platform, in which synthetic CAR targets (Tags) are produced and released in situ by tumor-colonizing probiotic bacteria (*E. coli* Nissle 1917) to label ubiquitous components of solid tumors for de novo lysis by GFP-CARs (GFP28z). Tags are designed as dimers of sfGFP fused to an HBD (PIGF<sub>123-144</sub>) that broadly bind to cell surface and matrix proteins found in the TME. (B) Representative flow cytometry histograms demonstrating GFP28z surface expression through binding purified sfGFP (left) and coexpression of mScarlet (right) in primary human T cells. (C) Flow cytometric quantification of CD25 surface expression after exposure to 100 ng/ml of GFP-based CAR targets for 16 hours—monomeric sfGFP (GFP), soluble diGFP, collagen-bound GFP (Tag)—shown relative to MDA-MB-468 cells expressing mbGFP at a 1:1 ratio. Data represent mean ± SD of *n* = 3 biological replicates. MFI, mean fluorescence intensity. (D) Representative flow cytometry histograms of surface-bound GFP after incubation with 500 ng/ml Tag-GFP or diGFP for 20 min. (E) Confocal microscopy images of Jurkats

expressing GFP28z-mScarlet fusion receptors for subcellular visualization. CARs are shown in orange and cocultured with unlabeled MDA-MB-468 target cells; images were acquired every 2 to 5 min after addition of 100 ng/ml of purified Tag. White arrows indicate CAR clusters. (F) Overnight killing assay against fLuc<sup>+</sup> HEK293T target cells at defined E:T ratios. CAR-T cells were cocultured with target cells ± 100 ng/ml of CAR targets for 20 hours. Specific lysis (%) was determined by normalizing relative light units (RLU) to cocultures with UT T cells. Data represent mean ± SD of *n* = 3 biological replicates. (G) Overnight killing assay of fLuc<sup>+</sup> HEK293T target cells at a 3:1 E:T with half log dilutions of purified Tag. Data represent mean ± SD of *n* = 3 biological replicates. (H) Overnight killing assays against a panel of fLuc<sup>+</sup> target cells at a fixed E:T ratio (3:1) and treated as in (F). (I) Overnight killing assay of fLuc<sup>+</sup> MDA-MB-468 in the presence of 20 ng/ml human HSPE (hHSPE) at a 1:1 E:T ratio, ± 100 ng/ml Tag. Data represent mean ± SD of *n* = 3 biological replicates. \*\*\**P* < 0.001; \*\*\*\**P* < 0.0001; two-way analysis of variance (ANOVA) [(C), (F), (H), and (I)] or one-way ANOVA (G), Holm-Sidak multiple comparison correction. ns, not significant; 468, MDA-MB-468.

binding of additional mouse lymphocyte and myeloid immune effector cells relative to mouse colorectal cancer cells (fig. S4B). We then hypothesized that surface-bound Tags may indeed facilitate synapse formation between CARs and the target cell; thus, we engineered an additional GFP28z receptor with a C-terminal mScarlet fusion to track CAR receptor localization by confocal microscopy. Notably, by 30 min after addition of purified Tag, GFP28z-mScarlet receptors appeared to cluster at the interface between each T cell and target cell, whereas T cells supplied with soluble diGFP and un-

treated cells remained unchanged (Fig. 1E and fig. S5, A and B).

In line with these findings, we observed minimal cytotoxic activity of GFP28z in response to phosphate-buffered saline (PBS) or diGFP in killing assays of *ffLuc*<sup>+</sup> human embryonic kidney (HEK) 293T cells at multiple effector-to-target (E:T) ratios. Conversely, GFP28z cells provided with Tags were able to drive significant levels of target cell lysis at high and low E:T ratios (Fig. 1F). We confirmed that this is a dose-dependent response, whereas cytotoxicity was still observable at Tag concentrations as

low as 1.5 ng/ml (Fig. 1G). Moreover, this combination achieved significant lysis across a panel of seven genetically distinct human cancer cell lines (Fig. 1H) while demonstrating no added effect on conventional CD19 (1928z)- or intercellular adhesion molecule-1 (ICAM-1) (ICAM28z)-directed CAR-T cells (fig. S6, A and B). We next measured the surface expression of CD107a—a membrane-bound molecule commonly used as a proxy for cytotoxic degranulation—and found higher expression on GFP28z incubated with collagen-bound Tags than cells exposed to diGFP (fig. S6C). Correspondingly, we detected

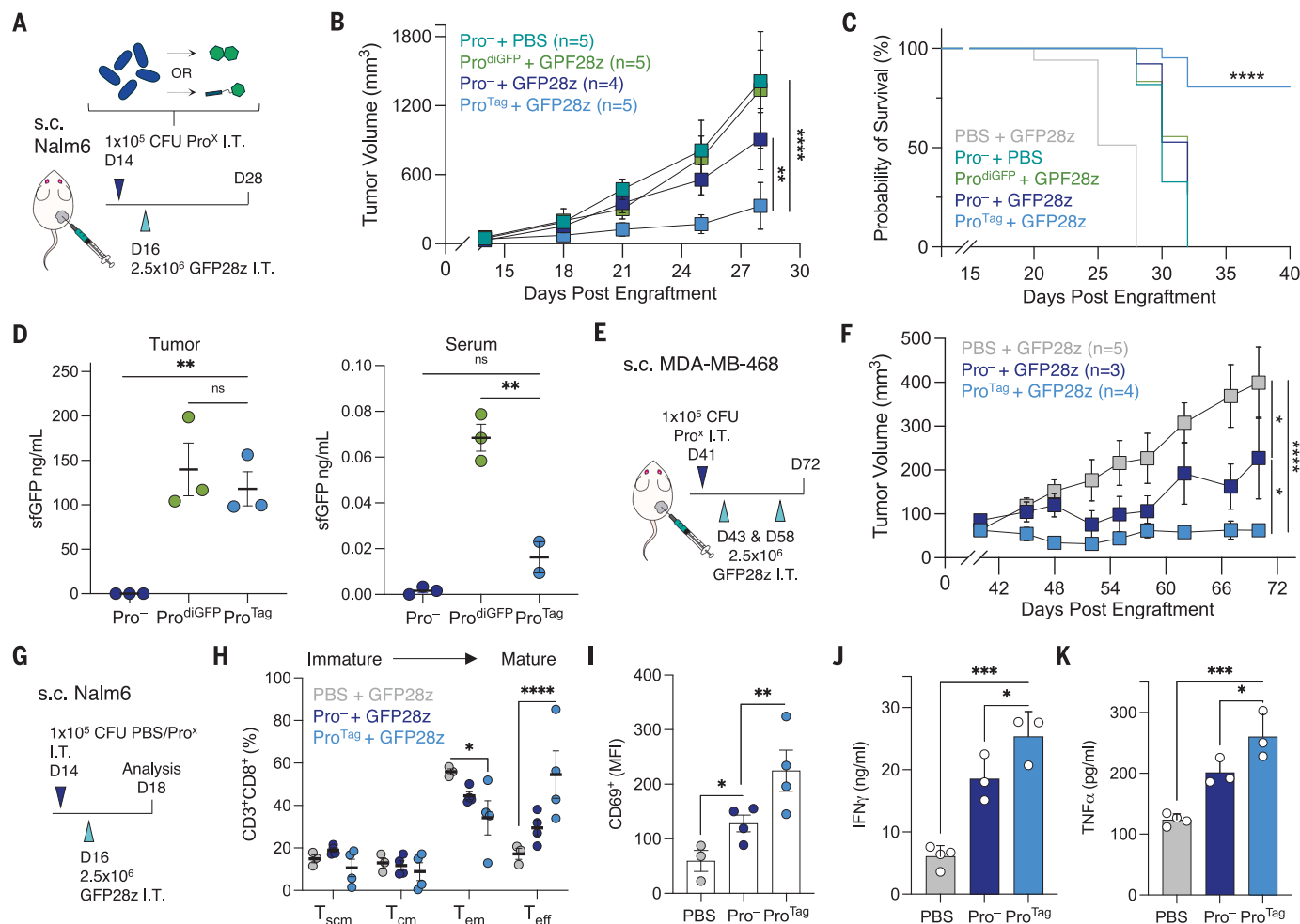


**Fig. 2. ProCAR-T cells yield antigen-agnostic therapeutic efficacy in response to Tags and bacterial adjuvants provided by probiotics in situ.**

(A to C) Nalm6 cells ( $5 \times 10^6$ ) were implanted subcutaneously ("s.c.") into the hind flank of NSG mice. When tumor volumes reached  $\sim 100$  mm<sup>3</sup>, mice were intratumorally injected with  $1 \times 10^5$  CFU of engineered probiotic strains (Pro<sup>X</sup>) producing diGFP (Pro<sup>diGFP</sup>) or Tag (Pro<sup>Tag</sup>) targets or an empty control (Pro<sup>-</sup>) (A). Then,  $2.5 \times 10^6$  GFP28z<sup>+</sup> ProCAR-T cells were delivered 48 hours post bacteria treatment (pbt), with tumor growth monitored by caliper measurements every 3 to 4 days. Mean tumor trajectories (B) and survival curves (C) are shown. Data represent mean  $\pm$  SEM of  $n > 4$  biological replicates. (D) ELISA quantification of sGFP levels from tumor homogenates (left) and serum (right) on day 14 pbt; data represent SEM of  $n = 3$  biological replicates. (E and F) MDA-MB-468 cells ( $5 \times 10^6$ ) were subcutaneously implanted into the hind flank of NSG mice. When tumors reached palpable volume, mice were intratumorally injected with  $1 \times 10^5$  CFU of

Pro<sup>Tag</sup> or control Pro<sup>-</sup> strains or PBS. On days 2 and 15 pbt, tumors were treated with  $2.5 \times 10^6$  GFP28z<sup>+</sup> ProCAR-T cells, and tumor growth was measured as in (A). Mean tumor trajectories are shown (F). Data represent mean  $\pm$  SEM of  $n > 3$  biological replicates. (G to K) Nalm6 tumors were established and treated as in (A) and resected on day 2 after T cell treatment (day 4 pbt) for analysis by flow cytometry. (H) Frequency of IT hCD45<sup>+</sup>CD3<sup>+</sup>CD8<sup>+</sup> T cell memory and effector populations determined by CD62L and CD45RO expression patterns. Data represent mean  $\pm$  SEM of  $n > 3$  biological replicates. (I) Flow cytometric quantification of CD69 surface expression on IT hCD45<sup>+</sup>CD3<sup>+</sup>CD8<sup>+</sup> cells in each treatment group. Data represent mean  $\pm$  SEM of  $n = 3$  biological replicates. (J and K) Luminex quantification of IT IFN- $\gamma$  (J) and TNF- $\alpha$  (K) concentrations. Data represent mean  $\pm$  SD of biological replicates. \* $P < 0.05$ ; \*\* $P < 0.01$ ; \*\*\* $P < 0.001$ ; \*\*\*\* $P < 0.0001$ ; two-way ANOVA [(B), (F), and (H)], log-rank test (C), or one-way ANOVA [(D), (I) to (K)], with Holm-Sidak multiple comparison correction.

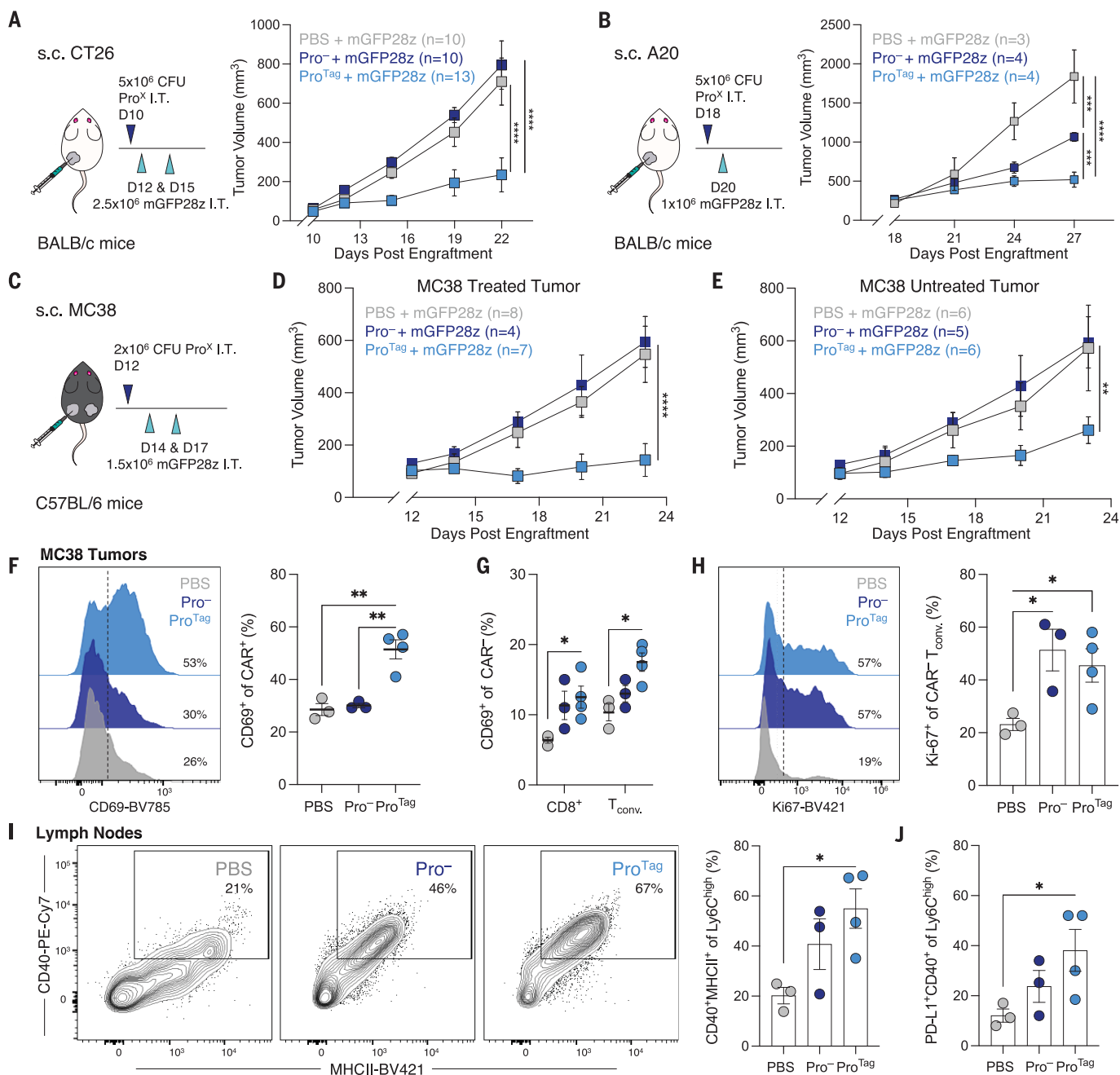


**Fig. 3. Treatment with the ProCAR platform provides a systemic therapeutic benefit in an immune-competent model of colorectal cancer.** (A) CT26 cells ( $5 \times 10^5$ ) were implanted subcutaneously into the hind flank of BALB/c mice. When tumor volumes reached  $\sim 100 \text{ mm}^3$ , mice were treated with  $5 \times 10^6$  CFU of engineered probiotic strains (Pro<sup>X</sup>) producing Tag (Pro<sup>Tag</sup>) or an empty control (Pro<sup>-</sup>). On days 2 and 5 pbt, tumors were treated with  $2.5 \times 10^6$  mGFP28z<sup>+</sup> T cells, and growth was monitored by caliper measurements every 3 to 4 days. Mean tumor trajectories are shown. Data represent mean  $\pm$  SEM of  $n > 10$  biological replicates. (B) A20 cells ( $5 \times 10^5$ ) were implanted subcutaneously into the hind flank of BALB/c mice. When tumor volumes reached 200 to  $300 \text{ mm}^3$ , mice were treated with probiotics as in (A). On day 2 pbt, tumors were treated with  $1 \times 10^6$  mGFP28z<sup>+</sup> T cells. Mean tumor trajectories are shown. Data represent mean  $\pm$  SEM of  $n > 3$  biological replicates. (C to E) MC38 cells ( $5 \times 10^5$ ) were implanted subcutaneously into both hind flanks of C57BL/6 mice. When tumor volumes reached  $\sim 150 \text{ mm}^3$ , the left tumor received a single injection of  $2 \times 10^6$  CFU Pro<sup>Tag</sup>, Pro<sup>-</sup>, or a PBS control (C). On days 2 and 5 pbt,

tumors on the left flank were treated with  $1.5 \times 10^6$  mGFP28z<sup>+</sup> T cells. Tumors on the right flank were left untreated. Mean tumor trajectories of the treated tumors (D) and untreated tumors (E) are shown. Data represent mean  $\pm$  SEM of  $n > 4$  biological replicates. (F to J) C57BL/6 mice were grafted and treated as in (C). On day 9 pbt, treated tumors and tumor-draining lymph nodes were retrieved for analysis by flow cytometry. (F) Frequency of IT CD69<sup>+</sup>CAR<sup>+</sup> T cells; representative flow cytometry histograms (left) and quantification are shown (right). Data represent mean  $\pm$  SEM of  $n > 3$  biological replicates. (G) Frequencies of CD69<sup>+</sup> tumor infiltrating CD8<sup>+</sup> and CD4<sup>+</sup>Foxp3<sup>+</sup> (T<sub>conv</sub>) CAR<sup>+</sup> T cells. Data represent mean  $\pm$  SEM of  $n > 3$  biological replicates. (H) Frequency of Ki-67<sup>+</sup> tumor-infiltrating CAR<sup>+</sup>CD8<sup>+</sup> T cells from each treatment group. (I and J) Frequency of activated (CD40<sup>+</sup>MHCII<sup>+</sup>) (I) and PD-L1<sup>+</sup> (J) proinflammatory monocytes (CD11b<sup>+</sup>Ly6C<sup>+</sup>) in the lymph nodes of treated and control mice. Data represent mean  $\pm$  SEM of  $n > 3$  biological replicates. \* $P < 0.05$ ; \*\* $P < 0.01$ ; \*\*\*\* $P < 0.0001$ ; two-way ANOVA [(A), (B), (D), (E), and (G)] or one-way ANOVA [(F), (H), (I), and (J)]; ANOVAs performed with Holm-Sidak multiple comparison correction.



higher levels of perforin and granzymes A and B in the supernatant of these cells, which together indicate direct mechanisms of cytotoxicity (fig. S6D).

We then sought to assess the importance of general matrix and adhesion molecules to the observed phenotype by incubating cancer cell lines with Tags after trypsinization. As anticipated, we observed a significant reduction in the level of surface-bound-GFP after trypsin-mediated cleavage of adhesion proteins (fig. S6E). Thus, we next considered the specific contribution of cell surface heparan sulfates (HSs) and HSPGs as a mechanism of direct cell interaction. Indeed, incubation with heparinase (HSPE) and cleavage of HS chains significantly disrupted the lysis of MDA-MB-468 cells by GFP28z, whereas the cytotoxic activity of 1928z was not inhibited by HSPE in a killing assay of Nalm6 cells (Fig. 1I and fig. S6F). Taken together, these results suggest that the Tag design confers broad utility that facilitates antigen-agnostic CAR activity.

#### **ProCAR system mediates antigen-agnostic therapeutic efficacy in human xenograft models**

Motivated by the cytotoxicity observed *in vitro*, we sought to characterize the full effects of the ProCAR platform *in vivo*, first by using non-obese diabetic scid gamma (NSG) mice bearing subcutaneous Nalm6 tumors. We have previously shown that EcN-SLIC (Pro<sup>X</sup>) strains can exclusively grow to a critical population density within the tumor core, synchronously lyse, and cyclically release therapeutic payloads every 48 to 72 hours after a single intratumoral (IT) injection (35). Therefore, we chose to treat tumors with a single IT injection of  $1 \times 10^5$  colony-forming units (CFU) of Pro<sup>X</sup> strains either producing diGFP (Pro<sup>diGFP</sup>) or Tag (Pro<sup>Tag</sup>) targets, or an empty control (Pro<sup>-</sup>), 48 hours before IT delivery of  $2.5 \times 10^6$  GFP28z<sup>+</sup> cells (Fig. 2A). Here, GFP28z in combination with Pro<sup>diGFP</sup> demonstrated no appreciable therapeutic efficacy and did not slow tumor growth compared with tumors treated with control Pro<sup>-</sup> strains alone (Fig. 2B and fig. S7A). By contrast, Pro<sup>Tag</sup> strains mediated potent anti-tumor responses, which achieved significantly slowed tumor growth and correspondingly improved survival (Fig. 2C).

We monitored the body weight of mice as a proxy for mouse health from the start of bacteria treatment and observed no significant weight loss in mice treated with Pro<sup>-</sup> alone, GFP28z alone, or any combination of the two cell therapies (fig. S7B). Additionally, we did not detect bacterial growth outside of tumor homogenates on day 3 and 14 post-bacteria treatment (pbt) (fig. S7C) and found that Tag-expression plasmids were well maintained *in vivo* (fig. S7D). To assess the tumor retention of probiotically delivered CAR targets, we quantified the level of GFP in tumor homogenates and matched serum samples from mice treated

with Pro<sup>-</sup>, Pro<sup>diGFP</sup>, and Pro<sup>Tag</sup> strains through GFP-specific enzyme-linked immunosorbent assay (ELISA). We detected comparable levels of both CAR targets in tumor homogenates across Pro<sup>diGFP</sup> and Pro<sup>Tag</sup> groups (Fig. 2D, left), which suggests that the observable differences in efficacy were the result not of unequal target abundance but rather of the ability of Tags to promote target cell killing when soluble targets do not. Furthermore, higher concentrations of sfGFP were detected in the serum of mice treated with Pro<sup>diGFP</sup>, which suggests that Tags reduce leakage into systemic circulation (Fig. 2D, right). To assess off-tumor Tag abundance directly, we quantified GFP concentration in tumor, lung, kidney, spleen, and liver homogenates from mice bearing subcutaneous HCT116 tumors and did not detect appreciable levels of GFP or bacterial growth in any healthy organ 14 days pbt (fig. S8, A to D).

We next considered the antigen-agnostic capability of the ProCAR platform and assessed therapeutic efficacy in a mouse model of human TNBC. Notably, TNBC tumors lack estrogen and progesterone receptors as well as HER2 expression, which makes them unresponsive to available targeted therapies and an opportunity for new treatment options (43). For initial assessment, mice bearing subcutaneous MDA-MB-468 tumors were treated with an IT injection of Pro<sup>X</sup> strains or PBS 2 days before receiving an IT injection of PBS, GFP28z, or control ICAM28z CAR-T cells. ProCARs responding to Pro<sup>Tag</sup> demonstrated enhanced antitumor efficacy relative to ICAM28z despite high ICAM-1 surface expression (fig. S9, A to C) (44), likely owing to the presence of potent Toll-like receptor (TLR) agonists inherent to the ProCAR system.

By day 28 after treatment, we observed signs of T cell dysfunction across all treatment groups (fig. S9E) despite the preserved bacterial lysis behavior and GFP production observed in Pro<sup>Tag</sup> isolates (fig. S9F). Therefore, to mitigate T cell exhaustion, we increased the frequency of T cell treatments to two doses, spaced 2 weeks apart while keeping to a single dose of probiotics. After this, the ProCAR system achieved durable anti-tumor efficacy, with no tumor growth observed for 70 days after engraftment (Fig. 2, E and F; fig. S10A). Moreover, treatment of an additional subcutaneous SKOV3 tumor model with ProCAR-T cells in combination with Pro<sup>Tag</sup> significantly slowed tumor growth (fig. S10, B and C).

Although we did not observe nonspecific effects from the presence of Pro<sup>Tag</sup> strains on UT T cells (fig. S10, D and E), we consistently noted moderate and model-independent activity of ProCAR-T cells in combination with control Pro<sup>-</sup> strains. Notably, activated T cells up-regulate TLR4 and TLR5 expression (45, 46), of which lipopolysaccharides (LPSs) and flagellin found on EcN are the respective agonists. Therefore, we hypothesized that IT bacteria may serve as an adjuvant to enhance ProCAR-T cell activity

(fig. S11A). To test this *in vitro*, we monitored the surface expression of CD69, CD25, and CD107a on GFP28z cells exposed to Pro<sup>-</sup> lysate or Tags separately, or the combination of both stimuli. GFP28z demonstrated significantly increased levels of all three markers in response to lysate alone, which indicates TLR stimulation, whereas the combination of lysate and collagen-bound Tags stimulated the highest expression (fig. S11B). This combination effect was also mirrored in the levels of proinflammatory cytokines detected in cell culture supernatants and in the enrichment of T<sub>eff</sub> populations, which demonstrates a strong shift toward cytotoxic effector functions (fig. S11, C and D).

To study the effects of CAR targets produced by live bacteria, we investigated the phenotype of GFP28z isolated from Nalm6 tumors on day 4 after treatment with PBS, Pro<sup>-</sup>, or Pro<sup>Tag</sup> (Fig. 2G). CD8<sup>+</sup> GFP28z T cells from Pro<sup>Tag</sup>-treated tumors were again significantly enriched for differentiated T<sub>eff</sub> populations, whereas cells from Pro<sup>-</sup>-treated tumors displayed a more modest trend toward differentiation relative to PBS-treated, or even purified Tag-treated, controls (Fig. 2H and fig. S12A). As a measure of activation, GFP28z cells displayed significantly increased CD69 and CD25 expression in response to Pro<sup>-</sup> and Pro<sup>Tag</sup> strains (Fig. 2I and fig. S12B). Correspondingly, tumors treated with either strain were found to contain significantly increased levels of human proinflammatory cytokines (Fig. 2, J and K, and fig. S12C), whereas the early exhaustion phenotype of GFP28z was found to be inversely correlated with exposure to bacteria, which demonstrates the potential benefit of MyD88 signaling after TLR activation (47) (fig. S12D). Together, these observations highlight the use of tumor-colonizing bacteria to mediate antigen-agnostic CAR-T cell activity while simultaneously boosting T cell effector functions through natural TLR stimulation.

#### **Treatment with the ProCAR platform provides a systemic therapeutic benefit in an immune-replete model of colorectal carcinoma**

Although the use of immunocompromised mice allows for the study of human T cell behavior in a bacterial platform, we next aimed to understand the performance of the ProCAR platform in the context of a functional immune system and comprehensive TME. To do this, we generated a GFP CAR using the same sfGFP-specific nanobody fused to the signaling components of mouse CD28 and CD3z (mGFP28z) for expression in mouse T cells and confirmed efficient killing of mbGFP-MC38 target cells (fig. S13, A and B). Consistent with our observations of human GFP28z, mouse CAR-T cells were strongly activated by collagen-bound Tag (fig. S13, C and D) and were able to drive the lysis of mouse TNBC and colorectal cancer cell lines through direct interaction with Tag and the target cell surface (fig. S13, E and F).

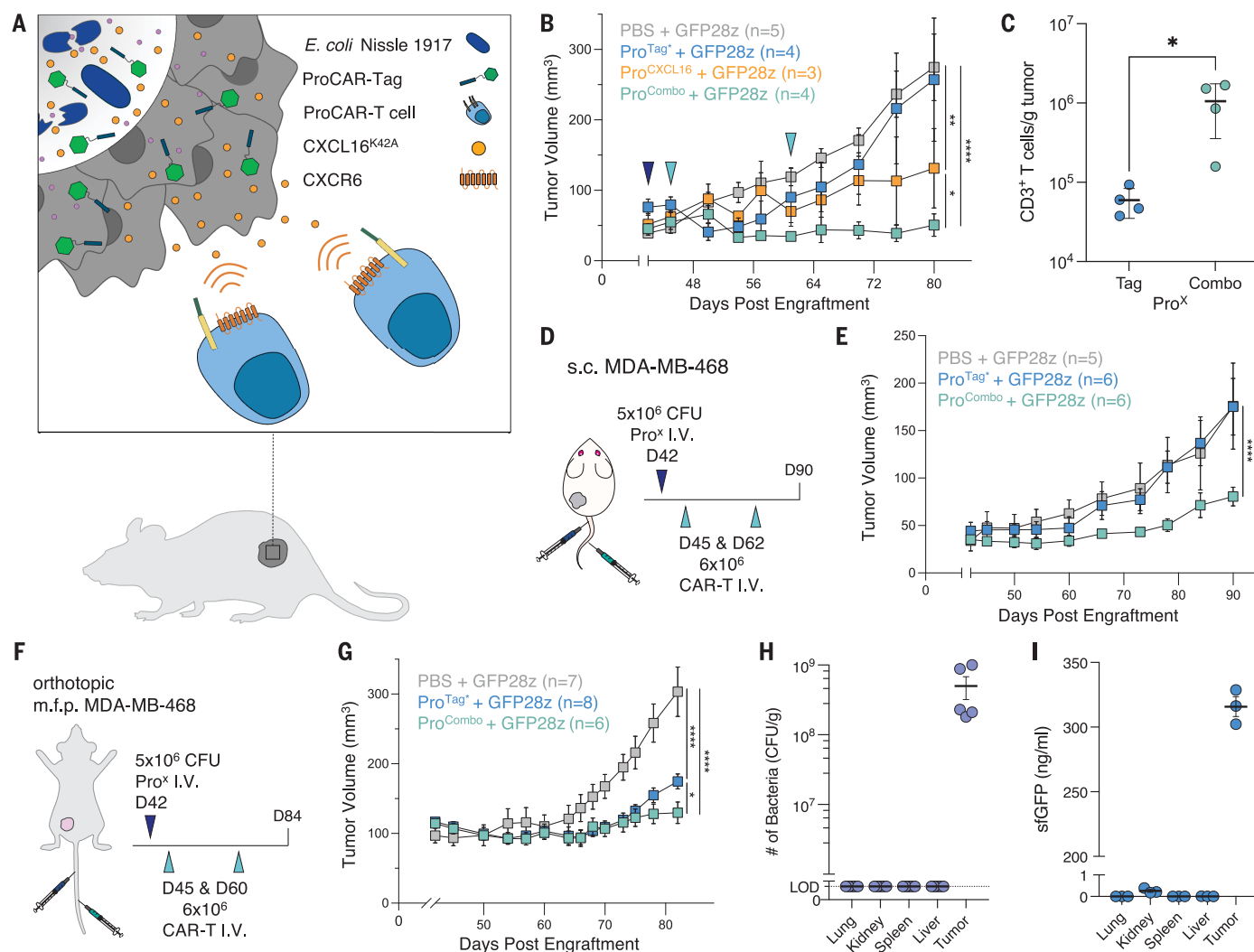


**Fig. 4. Multifunctional probiotics produce combinations of TME-modulating factors to facilitate systemic delivery and delay the growth of orthotopic breast tumors.**

(A) Probiotics are engineered to release an activating mutant of the human chemokine, CXCL16<sup>K42A</sup> ("CXCL16"), to recruit CXCR6<sup>+</sup> ProCAR-T cells directly to the tumor site. (B) MDA-MB-468 cells ( $5 \times 10^6$ ) were subcutaneously implanted into the hind flank of NSG mice. Palpable tumors were then either injected with  $1 \times 10^5$  CFU of a strain engineered to produce both CXCL16 and Tag in combination (Pro<sup>Combo</sup>), control strains producing single agents (Pro<sup>Tag</sup>, Pro<sup>CXCL16</sup>), or a PBS control. On days 2 and 15 pbt, mice were intravenously treated with  $6 \times 10^6$  GFP28z<sup>+</sup> T cells. Mean tumor growth trajectories are shown. Data represent mean  $\pm$  SEM of  $n > 3$  biological replicates per group. (C) Counts of infiltrating hCD45<sup>+</sup>CD3<sup>+</sup> cells per milligram of tumor. MDA-MB-468 tumors were established and treated as in (A). On day 7 after treatment, tumors from Pro<sup>Tag</sup> and Pro<sup>Combo</sup> treatment groups were retrieved and homogenized for analysis by flow cytometry. Data represent mean  $\pm$  SEM of  $n = 4$  biological replicates per group. (D and E) MDA-MB-468 tumors were established and measured as in (B). When tumors reached

palpable size, mice were intravenously treated with  $5 \times 10^6$  CFU of Pro<sup>X</sup> strains or PBS. On days 3 and 17 pbt, mice were intravenously treated with  $6 \times 10^6$  GFP28z<sup>+</sup> ProCAR-T cells. Mean tumor trajectories are shown (E). Data represent mean  $\pm$  SEM of  $n > 5$  biological replicates per group. I.V., intravenously. (F to I) An orthotopic model of TNBC was established through the surgical implantation of  $5 \times 10^6$  MDA-MB-468 cells into the mammary fat pad ("m.f.p.") of female NSG mice. When tumor volumes reached  $\sim 100$  mm<sup>3</sup>, mice were treated as in (D); mean tumor growth trajectories are shown (G). Data represent mean  $\pm$  SEM of  $n > 6$  biological replicates per group. (H and I) Biodistribution assessment of Pro<sup>X</sup> (H) and sfGFP (I) in tumor, lung, kidney, spleen, and liver homogenates. On day 42 pbt, tumor and matched healthy tissue were digested and plated with the appropriate antibiotics for colony quantification or assessed by ELISA for sfGFP concentration. Data represent mean  $\pm$  SEM of  $n = 5$  (H) or  $n = 3$  (I) biological replicates per group. Limit of detection (LOD), 200 CFU/g. \* $P < 0.05$ ; \*\* $P < 0.01$ ; \*\*\*\* $P < 0.0001$ ; two-way or one-way (C) ANOVA, with Holm-Sidak multiple comparison correction.

With the mouse components in hand, we initially sought to test the platform in immune-competent BALB/c mice bearing subcutaneous CT26 colorectal carcinomas. We dosed tumors directly with  $2 \times 10^6$  CFU of Pro<sup>-</sup> or Pro<sup>Tag</sup> alone or followed by two doses of autologous  $2.5 \times$

$10^6$  mGFP28z<sup>+</sup> T cells spaced 6 days apart. Notably, treatment with Pro<sup>Tag</sup> alone was not sufficient to generate an appreciable antitumor response without the co-delivery of mGFP28z, whereas the combination significantly slowed tumor progression (fig. S14, A and B). Moreover,

decreasing the time between T cell treatments to 3 days apart yielded significant antitumor efficacy that led to occurrences of tumor regression (Complete response CR = 3/13) and improved survival (Fig. 3A and fig. S14, C and D), whereas treatment with a single low dose

of mGFP28z ( $1 \times 10^6$ ) in combination with Pro<sup>Tag</sup> was able to control the growth of large A20 lymphomas (Fig. 3B and fig. S14E).

In these studies, we chose to omit the common practice of preconditioning lymphodepletion (48, 49) to observe any potential effects on the endogenous immune system. Thus, we aimed to investigate whether IT injection of the ProCAR system could generate signs of systemic antitumor immunity in a dual-flank MC38 colorectal carcinoma model established in C57BL/6 mice (Fig. 3C). Notably, we observed that unilateral treatment of one tumor not only resulted in instances of tumor regression on the treated side (CR = 2/7) but led to a significant reduction in the growth rate of distal, untreated tumors (Fig. 3, D and E, and fig. S14F). In contrast to the human system, we did not observe an appreciable effect of mGFP28z responding to control Pro<sup>-</sup> on either side, which suggests that mouse T cells may be less sensitive to TLR agonism.

To understand the underlying immune response, we next investigated the immunophenotype of cells isolated from the tumors and tumor-draining lymph nodes of treated and control mice (fig. S15A). Analogous to the human system, mGFP28z<sup>+</sup> T cells displayed the highest activation in response to Pro<sup>Tag</sup> treatment (Fig. 3F). As a measure of bystander T cell activation, we observed significantly increased CD69 expression on tumor-infiltrating CD8<sup>+</sup> and conventional CD4<sup>+</sup>Foxp3<sup>-</sup> (T<sub>conv</sub>) T cells in the CAR-negative CD3<sup>+</sup> fraction of Pro<sup>Tag</sup>-treated tumors (Fig. 3G). We also noted probiotic-related increases in the frequencies of Ki67<sup>+</sup> and CD44<sup>+</sup> tumor infiltrating T<sub>conv</sub> cells (Fig. 3H and fig. S15B), whereas analysis of the IT myeloid populations revealed increased frequencies of activated (CD40<sup>+</sup>MHCII<sup>+</sup>) monocytes (fig. S15C). Notably, we observed significantly expanded populations of activated and PD-L1<sup>+</sup> monocytes in the tumor-draining lymph nodes of treated mice (Fig. 3, I and J, and fig. S15D). Together, these data support the hypothesis that the cooperation between IT probiotics and activated CAR-T cells can propagate an adaptive response from the endogenous immune system, which ultimately leads to a systemic antitumor benefit.

#### **Multifunctional probiotics demonstrate selective colonization of human TNBC and yield therapeutic efficacy in orthotopic breast tumor models**

To advance the technology in an immunocompromised host, we pursued systemic delivery of human ProCAR-T cells by intravenous injection. Conventionally, CAR-T cell trafficking to solid tumors is often impeded by mismatched chemokine and receptor expression (50). Moreover, given the cyclical release of Tags relative to the constitutive surface expression of traditional TAAs, we hypothesized that circulating

GFP28z cells may have increased difficulty locating their target.

Thus, we equipped an additional strain with the mechanism to co-release an activating mutant of human CXCL16 (CXCL16<sup>K42A</sup>), in which lysine 42 is substituted with alanine) (51) and directly recruit ProCAR-T cells in circulation (Fig. 4A). Notably, CXCL16 is reported to interact exclusively with its cognate receptor, CXCR6, expressed on effector memory T cells (52). For this, we expressed CXCL16<sup>K42A</sup> and Tag genes from a single Axe/Txe stabilized vector under separate pTac and J23100 promoters (Pro<sup>Combo</sup>), respectively, and generated matched single control strains (Pro<sup>CXCL16</sup> and Pro<sup>Tag\*</sup>) with equivalent payload expression (fig. S16, A to C). As anticipated, treatment of subcutaneous TNBC tumors with the Pro<sup>Combo</sup> strain, followed by intravenous infusion of ProCAR-T cells, reduced tumor growth without affecting mouse body weight (Fig. 4B and fig. S16, D and E). Pro<sup>CXCL16</sup> also yielded an appreciable therapeutic benefit in this system, likely owing to the increased T cell infiltration and response to probiotic TLR agonists. Analysis of tumor homogenates revealed high and comparable payload expression and significantly increased hCD45<sup>+</sup>CD3<sup>+</sup> T cell counts in tumors treated with Pro<sup>Combo</sup> relative to tumors treated with Pro<sup>Tag\*</sup> alone (Fig. 4C and fig. S16, F and G), which together suggest that chemokine support is necessary for T cell recruitment and therapeutic efficacy in inaccessible subcutaneous tumors.

We then sought to assess the feasibility of delivering the complete ProCAR platform by systemic injection. We carefully monitored mouse health during a dose escalation study of intravenously delivered Pro<sup>-</sup> strains and noted that initial weight loss in response to higher CFUs was recovered by day 7 after treatment and that systemic delivery did not lead to bacterial growth in healthy organs despite achieving 100% tumor-colonization efficiency by 48 hours after infusion (fig. S17, A to E). With this information, we treated mice bearing subcutaneous TNBC tumors with a single intravenous dose of Pro<sup>Tag\*</sup> or Pro<sup>Combo</sup> strains at  $5 \times 10^5$  CFU, followed 72 hours later with the first infusion of ProCAR-T cells (Fig. 4, D and E). Again, tumors colonized by Pro<sup>Combo</sup> strains demonstrated significantly slowed growth relative to PBS and Pro<sup>Tag\*</sup> treatment groups without causing discernable signs of off-tumor toxicity (fig. S17, F to I).

Ultimately, we established an orthotopic model of TNBC through the surgical implantation of MDA-MB-468 cells into the mammary fat pad (MFP) of female NSG mice (Fig. 4F). In this model, intravenous infusion of the ProCAR system led to appreciable therapeutic efficacy in both Pro<sup>Tag\*</sup> and Pro<sup>Combo</sup> treatment groups, although Pro<sup>Combo</sup> provided enhanced therapeutic benefit (Fig. 4G and fig. S18, A and B). Moreover, we observed sim-

ilar probiotic colonization levels restricted to MFP tumors (Fig. 4H) and minimal off-tumor sfGFP expression in healthy organs (Fig. 4I). To specifically study the tissue distribution of Pro<sup>X</sup> and Tag within the MFP, we retrieved tumors and surrounding healthy tissue for immunohistochemical staining for *E. coli* and GFP (fig. S19). *E. coli* staining of tumor sections from Pro<sup>-</sup> and Pro<sup>Tag\*</sup> treatment groups revealed probiotic localization to the tumor core, with correspondingly strong GFP detection in the core of Pro<sup>Tag\*</sup> treated tumors. Moreover, hematoxylin and eosin sections of healthy organs taken from treated and untreated groups did not show evidence of tissue damage (fig. S20A). In addition, intravenous treatment in an immune-replete context did not yield signs of inflammatory organ damage in the serum of female Friend Virus B NIH Jackson FVB mice bearing syngeneic mammary specific polyomavirus middle T antigen overexpression mouse model (MMTV-PyMT) MFP tumors (fig. S20, B to D). Collectively, these mouse model data demonstrate the use of engineered probiotics to selectively grow within the TME niche and safely release combinations of CAR-T cell enhancing payloads in situ.

#### **Concluding remarks**

We have demonstrated an approach to engineering interactions between living therapies, in which tumor-colonizing probiotics have been repurposed to guide the cytotoxicity of engineered T cells. We have shown that by fusing synthetic CAR targets to an HBD, we can achieve antigen-agnostic cell death, and by harnessing the tumor-restricted growth of *E. coli*, we can release these targets directly within the TME to achieve efficacy in genetically distinct mouse models of human and mouse cancer. These findings highlight the potential of the ProCAR platform to address the roadblock of identifying suitable CAR targets by providing an antigen that is orthogonal to both healthy tissue and tumor genetics.

Notably, even the gold standard CD19 CAR faces antigen-dependent issues, the loss of which has become a frequent cause of patient relapse (7), and off-tumor expression on brain mural cells has been linked to reports of dangerous neurotoxicity (5). The antigen bottleneck appears to have a greater impact upon treatment of solid cancers, and approaches to overcome these issues have primarily relied on incorporating complex genetic circuitry to afford greater control over TAA recognition. Strategies targeting more than one antigen can circumvent issues of tumor escape (53, 54), yet the challenge of finding a single suitable target can limit this approach for most solid tumors.

Tumor pattern recognition (13) and Boolean-gated logic circuits (11) provide elegant solutions to the issue of off-tumor toxicity; however, they involve complex T cell engineering and



insertion of multiple transgenes. Other approaches to build universal CARs, in which the antigen recognition domain is provided by separate intravenous infusion, enables the exchange of antigen specificity during treatment (12). Additionally, CARs secreting bispecific T cell engagers (BiTEs) against broadly expressed targets have been effective in preclinical models of heterogeneous tumors (14). Although these strategies represent considerable advancements, such approaches rely on conventional target identification and tumor genetics. Thus, several groups have looked to nanoparticles, oncolytic viruses, and IT injection as alternative platforms to deliver CAR-T cell targets to solid tumors (17–21).

Here, the use of bacteria in the ProCAR system offers a partner organism that facilitates tumor-specific target delivery while concurrently providing natural inflammatory properties that serve to enhance the antitumor response. Our study in xenograft tumor models revealed a greater sensitivity of human T cells toward bacterial adjuvants, which demonstrates consistent antitumor benefits in response to control Pro<sup>+</sup> strains. By contrast, study of the ProCAR system in syngeneic tumor models demonstrated that a bacteria-based immunotherapy may be sufficient to prime systemic antitumor immunity in treated tumors, which can subsequently direct responses against uncolonized tumors or “untagged” tumor areas. Nonetheless, together these studies have demonstrated the tumor-specific growth of engineered probiotics in both immune-replete and immunocompromised mice, without the generation of apparent systemic infection or inflammatory damage.

Although not assessed here, humans are more sensitive to endotoxins than mice, and an important concern for clinical translation will be the potential toxicity from systemic administration of a Gram-negative bacterial therapy (55). Thus, a critical approach for translation will be to introduce genetic attenuations that have previously enabled both local and intravenous administration of bacterial therapies in clinical trials (33, 56). Structural modifications to LPSs have been shown to substantially reduce TLR4 stimulation without disrupting bacteria viability and tumor colonization (57, 58). Such attenuations could be combined with additional circuits to further restrict bacteria growth and reduce immunogenicity to facilitate safe systemic delivery and repeat dos-

ing (59, 60). Overall, combining the advantages of tumor-homing bacteria and CAR-T cells provides a new strategy for tumor recognition and, in turn, builds the foundation for engineered communities of living therapies.

## REFERENCES AND NOTES

1. A. Hyrenius-Wittsten, K. T. Roybal, *Trends Cancer* **5**, 583–592 (2019).
2. W. A. Lim, C. H. June, *Cell* **168**, 724–740 (2017).
3. N. Chen, X. Li, N. K. Chintala, Z. E. Tano, P. S. Adusumilli, *Curr. Opin. Immunol.* **51**, 103–110 (2018).
4. S. A. Richman et al., *Cancer Immunol. Res.* **6**, 36–46 (2018).
5. K. R. Parker et al., *Cell* **183**, 126–142.e17 (2020).
6. R. A. Morgan et al., *Mol. Ther.* **18**, 843–851 (2010).
7. R. G. Majzner, C. L. Mackall, *Cancer Discov.* **8**, 1219–1226 (2018).
8. D. M. O'Rourke et al., *Sci. Transl. Med.* **9**, eaaa0984 (2017).
9. I. C. Miller et al., *Nat. Biomed. Eng.* **5**, 1348–1359 (2021).
10. M. H. Abedi, J. Lee, D. I. Piraner, M. G. Shapiro, *ACS Synth. Biol.* **9**, 1941–1950 (2020).
11. K. T. Roybal et al., *Cell* **167**, 419–432.e16 (2016).
12. J. H. Cho, J. J. Collins, W. W. Wong, *Cell* **173**, 1426–1438.e11 (2018).
13. S. Sukumaran et al., *Cancer Discov.* **8**, 972–987 (2018).
14. B. D. Choi et al., *Nat. Biotechnol.* **37**, 1049–1058 (2019).
15. T. J. Gardner et al., *Nat. Chem. Biol.* **18**, 216–225 (2022).
16. L. Labanieh et al., *Cell* **185**, 1745–1763.e22 (2022).
17. A. Q. Zhang et al., *Nat. Biomed. Eng.* (2023).
18. X. Huang et al., *Nat. Nanotechnol.* **16**, 214–223 (2021).
19. A. K. Park et al., *Sci. Transl. Med.* **12**, eaaz1863 (2020).
20. A. Wing et al., *Cancer Immunol. Res.* **6**, 605–616 (2018).
21. L. Gamboa et al., *bioRxiv* 2021.12.11.472238 (2021). <https://doi.org/10.1101/2021.12.11.472238>.
22. N. S. Forbes, *Nat. Rev. Cancer* **10**, 785–794 (2010).
23. D. Nejman et al., *Science* **368**, 973–980 (2020).
24. G. D. Sepich-Poore et al., *Science* **371**, eabc4552 (2021).
25. C. Urbaniak et al., *Appl. Environ. Microbiol.* **80**, 3007–3014 (2014).
26. S. Zhou, C. Gravekamp, D. Bermudes, K. Liu, *Nat. Rev. Cancer* **18**, 727–743 (2018).
27. M. R. Wu, B. Jusiak, T. K. Lu, *Nat. Rev. Cancer* **19**, 187–195 (2019).
28. J. H. Zheng et al., *Sci. Transl. Med.* **9**, eaak9537 (2017).
29. L. B. Augustin et al., *J. Drug Target.* **29**, 430–438 (2021).
30. M. O. Din et al., *Nature* **536**, 81–85 (2016).
31. S. Chowdhury et al., *Nat. Med.* **25**, 1057–1063 (2019).
32. D. S. Leventhal et al., *Nat. Commun.* **11**, 2739 (2020).
33. J. F. Toso et al., *J. Clin. Oncol.* **20**, 142–152 (2002).
34. T. J. Gniadek et al., *J. Immunother.* **43**, 217–221 (2020).
35. C. R. Gurbatri et al., *Sci. Transl. Med.* **12**, eaax0876 (2020).
36. Z. L. Chang et al., *Nat. Chem. Biol.* **14**, 317–324 (2018).
37. M. M. Martino et al., *Science* **343**, 885–888 (2014).
38. N. Momin et al., *Sci. Transl. Med.* **11**, eaaw2614 (2019).
39. A. J. Davenport et al., *Proc. Natl. Acad. Sci. U.S.A.* **115**, E2068–E2076 (2018).
40. A. J. H. Fedorec et al., *iScience* **14**, 323–334 (2019).
41. A. Twair, S. Al-Oklia, M. Zarkawi, A. Q. Abbady, *Mol. Biol. Rep.* **41**, 6887–6898 (2014).
42. J. Wagner et al., *Cancer Immunol. Res.* **9**, 279–290 (2021).
43. P. Schmid et al., *N. Engl. J. Med.* **379**, 2108–2121 (2018).
44. P. Guo et al., *Proc. Natl. Acad. Sci. U.S.A.* **111**, 14710–14715 (2014).
45. G. Caron et al., *J. Immunol.* **175**, 1551–1557 (2005).

46. D. Geng et al., *Cancer Res.* **75**, 1959–1971 (2015).
47. M. Mata et al., *Cancer Discov.* **7**, 1306–1319 (2017).
48. J. P. Murad et al., *Mol. Ther.* **29**, 2335–2349 (2021).
49. C. Jin, J. Ma, M. Ramachandran, D. Yu, M. Essand, *Nat. Biomed. Eng.* **6**, 830–841 (2022).
50. M. Idorn et al., *Oncimmunology* **7**, e1450715 (2018).
51. T. M. Savage et al., *Sci. Adv.* **9**, eadc9436 (2023).
52. S. Lesch et al., *Nat. Biomed. Eng.* **5**, 1246–1260 (2021).
53. C. Chen et al., *Cancer Immunol. Immunother.* **66**, 475–489 (2017).
54. E. Zah, M. Y. Lin, A. Silva-Benedict, M. C. Jensen, Y. Y. Chen, *Cancer Immunol. Res.* **4**, 498–508 (2016).
55. S. Copeland et al., *Clin. Diagn. Lab. Immunol.* **12**, 60–67 (2005).
56. J. J. Luke et al., *Clin. Cancer Res.* **29**, 2435–2444 (2023).
57. B. D. Needham et al., *Proc. Natl. Acad. Sci. U.S.A.* **110**, 1464–1469 (2013).
58. J. Stritzker, P. J. Hill, I. Gentschev, A. A. Szalay, *Bioeng. Bugs* **1**, 139–145 (2010).
59. T. Harimoto et al., *Nat. Biotechnol.* **40**, 1259–1269 (2022).
60. T. Chen et al., *Nat. Biomed. Eng.* **6**, 94–104 (2022).

## ACKNOWLEDGMENTS

We thank M. Sadelain for providing the fLuc<sup>+</sup> Nalm6 acute lymphoblastic leukemia cell line, R. Schwabe for providing the Huh7 hepatoma cell line, and S. Acharyya for providing the PYMT-derived cell line. We thank N. Zervoudis and members of the Obermeyer group for expert assistance with protein purification. We thank M. J. Williams, S. Wyman, A. Sivan, and J. Hahn for critical review of the manuscript. We thank B. Fountaine and B. W. Johnson for their expert advice and histologic processing, immunohistochemistry, and imaging with the Histology and Imaging core at the University of Washington. We thank T. Swayne and E. L. Munteanu for their advice with confocal microscope image acquisition and analysis. Microscopy was performed with the Confocal and Specialized Microscopy Shared Resource of the Herbert Irving Comprehensive Cancer Center at Columbia University, funded in part through the NIH-NCI Cancer Center Support Grant P30CA013696. Flow cytometry and cell sorting was performed in the Columbia University Department of Microbiology and Immunology Flow Cytometry core facility and the Irving Institute's Biomarkers Core Laboratory. **Funding:** This work was supported by NIH 1R01EB030352 and U11 TR001873 and the NSF Graduate Research Fellowship (1644869 to C.R.G.). **Author contributions:** R.L.V. and T.D. conceived the study. R.L.V. designed and constructed the system and performed all in vitro experiments, T.S. assisted with confocal microscopy, and J.I. constructed the combination vector. R.L.V., F.L., C.R.G., A.V.C., M.R., E.R.B., K.S.A., J.I., M.K., L.B., and A.R. performed in vivo and/or ex vivo experiments. R.L.V., N.A., and T.D. wrote or edited the manuscript with input from all authors. **Competing interests:** R.L.V., T.S., C.R.G., J.I., N.A., and T.D. are inventors on a patent application describing the use of ProCAR-T cells for cancer immunotherapy (International Application no. PCT/US2022/016775). **Data and materials availability:** All data are available in the main text or supplementary materials. Correspondence and request for materials should be addressed to T.D. **License information:** Copyright © 2023 the authors, some rights reserved; exclusive licensee American Association for the Advancement of Science. No claim to original US government works. <https://www.sciencemag.org/about/science-licenses-journal-article-reuse>

## SUPPLEMENTARY MATERIALS

[science.org/doi/10.1126/science.add7034](https://science.org/doi/10.1126/science.add7034)  
Materials and Methods  
Figs. S1 to S20  
References (61–64)  
MDAR Reproducibility Checklist

Submitted 16 August 2022; resubmitted 22 June 2023  
Accepted 24 August 2023  
10.1126/science.add7034





## Probiotic-guided CAR-T cells for solid tumor targeting

Rosa L. Vincent, Candice R. Gurbatri, Fangda Li, Ana Vardoshvili, Courtney Coker, Jongwon Im, Edward R. Ballister, Mathieu Rouanne, Thomas Savage, Kenia de los Santos-Alexis, Andrew Redenti, Leonie Brockmann, Meghna Komaranchath, Nicholas Arpaia, and Tal Danino

*Science* **382** (6667), . DOI: 10.1126/science.add7034

### Editor's summary

Immunotherapy has proven highly efficacious for certain types of blood cancers, but the lower success rates for solid tumors remain a challenge. Vincent *et al.* designed probiotics that could home in and colonize solid tumors to improve chimeric antigen receptor (CAR) T cell immunotherapy. The two-step approach involved engineering a nonpathogenic strain of *Escherichia coli*, which delivered synthetic antigens to the tumor microenvironment and “tagged” the tumor (see the Perspective by Bressler and Wong). They next generated CAR T cells that were programmed to recognize these synthetic antigen tags. When the *E. coli* probiotic was administered, the CAR T cells could be directed to the solid tumors, where they orchestrated tumor cell killing in experimental models of breast and colon cancer. —Priscilla N. Kelly

### View the article online

<https://www.science.org/doi/10.1126/science.add7034>

### Permissions

<https://www.science.org/help/reprints-and-permissions>

Use of this article is subject to the [Terms of service](#)

*Science* (ISSN 1095-9203) is published by the American Association for the Advancement of Science. 1200 New York Avenue NW, Washington, DC 20005. The title *Science* is a registered trademark of AAAS.

Copyright © 2023 The Authors, some rights reserved; exclusive licensee American Association for the Advancement of Science. No claim to original U.S. Government Works